Check for updates

Orientation dependence of the fracture mechanisms in (V,Al)N coatings determined by micropillar compression

Markus R. Schoof[1,a)] , **James S. K.-L. Gibson[1], Soheil Karimi Aghda[2], Marcus Hans[2],**
Jochen M. Schneider[2], Sandra Korte-Kerzel[1]

[1] *Institute of Physical Metallurgy and Materials Physics, RWTH Aachen University, Kopernikusstraße 14, 52074 Aachen, Germany*
[2] *Materials Chemistry, RWTH Aachen University, Kopernikusstraße 10, 52074 Aachen, Germany*
a) Address all correspondence to this author. e-mail: schoof@imm.rwth-aachen.de

Transition metal aluminium nitrides produced by physical vapour deposition are widely used as hard, protective coatings in the manufacturing industries. To optimise coatings wear resistance while maintaining fracture toughness, an understanding of the mechanisms linking the microstructure and the orientation-dependent fracture behaviour is required. (V,Al)N coatings were synthesised by direct current and high power pulsed magnetron sputtering. Uniaxial compression testing was performed using micropillars oriented between 0° and 90° with respect to the growth direction to assess the effect of microstructure on the fracture behaviour. We show here that different fracture mechanisms are active depending on the alignment of grains and loading direction. The fracture behaviour could be divided into three classes associated with column buckling, decohesion or shearing and no significant difference between the specimens induced by the deposition process could be observed.

Introduction

Transition metal nitride (TMN) and boride protective coatings have already been valued for several years in technical processes because of their excellent properties, such as high hardness and elasticity [1–4], high thermal stability [5] and good electrical conductivity [6–8]. The application as thin protective layers deposited by physical vapour deposition (PVD) has therefore already been investigated towards its applicability for various industrial applications [9–12]. Used as a coating for tools, such as injection moulding machines or extruder barrels, TMN coatings are subjected to various axial and lateral forces. This can lead to deformation and thus to damage of the coating.

Within the last 20 years, high power pulsed magnetron sputtering (HPPMS) [13] has attracted interest for the industrial growth of protective coatings. Such plasmas are characterised by a significant fraction of metal ions [14], while gas ions dominate the plasma composition of direct current magnetron sputtering (DCMS) [15]. These metal ions in HPPMS allow for tailoring of the phase formation as well as densification and consequently enhance the mechanical properties [16]. Thin films produced by DCMS typically exhibit a lower density and higher surface

roughness as well as a higher deposition rate than those produced by HPPMS [17]. Furthermore, stronger magnets [18] and utilisation of a higher bias voltage in the HPPMS process [19] result in denser layers with lower roughness. Even if the density of the layer increases, the size of the grains is only slightly affected by the choice between DCMS and HPPMS or the strength of the magnets [18]. However, as the coating thickness increases, the density of the film decreases again and the roughness increases [18]. Two coatings with the same composition but deposited using different conditions or deposition processes then may or may not result in similar mechanical properties.

To study the mechanical behaviour of these coatings, a number of micro-mechanical test methods are in use. Some of these are briefly described below. Nevertheless, as explained later, they all leave room for improvement.

Measurements of hardness and stiffness of thin coatings are usually carried out by means of nanoindentation [20–24]. Several studies have investigated nitride systems similar to the (V,Al)N coatings used here, including the binary systems VN [1], CrN [25] and TiN [26] as well as the ternary systems (X,Al)N with X = V, Cr, Ti [1, 25, 27, 28], so that Young's

modulus, and hardness are known in addition to lattice parameters. It was found that thin films usually have a slightly higher hardness than the corresponding bulk material [29] and the cubic ternary films with higher Al content also show a higher hardness [5, 29, 30] but a more brittle behaviour [31] as long as they have the same crystal structure. A correlation between the structure and the mechanical properties was also shown using the H^3/E^2 ratio as an indicator [32]. In their study Musil et al. [32] found that for a protective layer its resistance against cracking is more important than its toughness and it was shown, that for hard coatings an increasing H^3/E^2 ratio up to 0.6 GPa was related to an increase of the resistance to cracking [32].

To describe the fracture behaviour, the fracture toughness is commonly used and even though Malzbender et al. [33] have already shown that the fracture toughness can also be estimated by means of nanoindentation which is affected by the residual stress state [34], the micro-beam bending method is usually used. First described by Wurster et al. [35] using elastic plastic fracture mechanisms (EPFM), the effects of the size and geometry of the bending beams have been highlighted in a number of investigations [36–39]. These methods allow observation of crack propagation in situ and to establish a relationship between stiffness and crack length [40, 41]. Furthermore, the critical crack energy for crack initiation of hard thin films could be calculated by means of cantilever deflection [42, 43]. Fracture toughness tests have been carried out on nitride coatings with different chemical compositions, such as (V,Al)N, (Ti,Al)N [44]. The effect of chemistry is less clear, and may be substrate dependent, with coatings on copper showing that (Ti,Al)N has a higher fracture toughness than (V,Al)N [45], while coatings on silicon showed the reverse [44]. Other experiments on TiN and (Ti,Al)N exhibited scatter in the fracture toughness [46, 47] depending on microstructure and heat treatment. However, these tests are very expensive and time-consuming, particularly where the microcantilevers are prepared by focussed ion beam milling and deformed inside an electron microscope. Simpler and faster methods are therefore often used instead, even though they are less quantitative, such as crack density measurements [45], Rockwell impact or scratch tests.

Investigations using scratch and Rockwell impact tests have shown that even brittle nitride coatings undergo plastic deformation not only under hydrostatic, concentrated loads as in indentation, but also under similar but dynamic loading conditions. The adhesion behaviour between coating and substrate can also be investigated in this way [12, 48–51], but several studies suggest that the mechanical properties of the coating, the tribological behaviour and the substrate/coating interface are interrelated [32, 52]. For example, high resistance to plastic deformation also leads to improved abrasion resistance at the substrate/coating interface [52]. To guide materials and process design, it is therefore important to characterise the coating itself, ideally revealing also the different possible fracture mechanisms individually with their respective critical stresses.

Originally introduced to investigate the size effect on strength, micro compression tests have proved to be an effective mean of investigating plasticity in brittle materials, as by scaling down the test, premature cracking can be avoided and stresses can be selectively applied to individual slip systems [53, 54]. Using a stress concentration to induce splitting, fracture has also been investigated using micropillars [55–57]. Another advantage in micro compression tests is that residual stresses in coatings are almost relieved in the form of micropillars [58].

Here micropillar compression is used as a method to selectively look at the individual failure mechanisms. As the method combines small sample volume, short preparation times and directional stress, it provides potential to efficiently assess the orientation-dependent fracture properties of brittle thin films. (V,Al)N coatings were chosen for investigation because they exhibited the highest Young's modulus and fracture toughness in a previous study [44] compared to the rest of the material systems investigated. Furthermore, (V,Al)N showed the typical columnar growth for both deposition processes.

Experiments

Coating synthesis, composition and phase formation

(V,Al)N coatings were deposited on 10×10 mm^2 Si(001) substrates in an industrial scale CemeCon CC 800/9 (Würselen, Germany) deposition system with utilisation of two Melec SIPP2000USB-10-500-S pulsers and 10 kW ADL GX 100/1000 DC power supplies. V and Al targets ($> 99.7\%$ purity) were assembled from two triangular pieces forming rectangular plates with dimensions 8.8×50 cm^2. Substrates were ultrasonically cleaned in acetone and ethanol for 10 min prior to loading to the chamber and were mounted on a copper holder facing the targets. The angles between the targets and substrate normal were ~ 27° and the target-to-substrate distance was 10 cm. The substrate temperature was kept at ~ 450 °C during the depositions and the base pressure of the chamber prior to the depositions was below 0.7 mPa. A total pressure of 0.44 Pa was employed for sputtering with a constant Ar:N$_2$ flow rate ratio of 2:1. Two different powering schemes were employed to deposit two series of (V,Al)N coatings.

In the first series, both targets were operated in DCMS mode (V/Al-DCMS) with the average powers of 2.4 kW for V target and 2.5 kW for Al target which resulted in similar power densities of 6.9 W/cm^2. A continuous DCMS bias

voltage of − 70 V was employed throughout the deposition. The deposition time was 90 min resulting in the film thickness of ∼ 3.0 μm. In the second powering scheme, each target was operated by separate HPPMS power supplies, each using pulse on-time of $\tau_{\text{HPPMS}} = 50$ μs at a duty cycle of 2.5% corresponding to a pulsing frequency of $f = 500$ Hz. Time-average powers of 2.4 kW for the V target and 2.5 kW for the Al target, similar to the DCMS mode, were used, which resulted in the peak power densities of 615 W/cm^2 and 510 W/cm^2 for the V and Al targets, respectively. A pulsed substrate bias potential of − 70 V was used to enhance the densification of the films [19]. The pulse on-time of the bias potential was $\tau_{\text{s}} = 100$ μs synchronised with the HPPMS pulses at the targets with + 30 μs phase shift to prevent acceleration of the gas ions generated at the beginning of the pulses [16]. Film thickness of ∼ 2.7 μm was obtained for the 135-min-long V/Al-HPPMS deposition.

The coating microstructure was characterised using scanning transmission electron microscopy (STEM). Cross-sectional lamellae were prepared by focussed ion beam (FIB) techniques in an FEI Helios Nanolab 660 dual-beam microscope (Hillsboro, OR, USA). This microscope was also used for acquiring bright field (BF) images with a STEM III detector at acceleration voltage and current of 30 kV and 50 pA, respectively. The chemical composition was determined by energy dispersive X-ray spectroscopy (EDX) using a JEOL JSM-6480 scanning electron microscope with an EDAX Genesis 2000 detection system at 12 kV acceleration voltage. A coating analysed by time-of-flight elastic recoil detection served as standard [19]. Structural analysis was performed using a Bruker AXS D8 Discover General Area Detection Diffraction System (Billerica, MA, USA) with an incident angle of 15°. A Cu Kα radiation source was used at a voltage and current of 40 kV and 40 mA, respectively. X-ray stress analysis was done utilising the sin$^2\psi$ method in a psi geometry (ψ tilt axis in the diffraction plane), assuming a biaxial stress state [59]. Young's modulus E and nanoindentation hardness H were obtained in a Hysitron (Minneapolis, MN, USA) TI-900 TriboIndenter equipped with a Berkovich geometry diamond tip with 100 nm radius. For each sample, 80 quasistatic indents were performed, which resulted in contact depths of < 5% with respect to the film thickness. A fused silica standard was used to determine the tip area function. Load–displacement curves were analysed using the method of Oliver and Pharr [21].

Size and load rate effects

To determine the effects of strain rate or micropillar geometry, tests were performed on the coating grown by HPPMS with tilt angles of 0°, 30° and 90°.

Two test series were performed: In one set of tests the load rate was varied from 0.1 to 1.0 mN/s, which covered a range of strain rates between 0.4×10^{-3} and 3.5×10^{-3} s^{-1}. In a second test series a load rate of 1.0 mN/s was chosen and the diameter of the micropillar varied between 0.5 and 1.25 μm with a constant height to diameter ratio of $\alpha = 2{:}1$.

Compression of micropillars tilted to column growth direction

The fracture behaviour of micropillars with aligned columns was determined by compression tests on micropillars with a tilt angle between 0° and 90°. The tilt was varied in 10° steps. At all tilt angles, a load rate of 1.0 mN/s and a diameter of 1.0 μm was used based upon the results obtained from the tests described in section 'Size and strain rate effects'.

All micro compression tests described in section 'Compression of micropillars tilted to column growth direction' were performed using an iNano nanoindenter (Nanomechanics Inc., TN, USA) and a 10 μm diamond flat punch provided by Synton MDP, Switzerland. For each datapoint reported, between 4 and 7 micropillars were compressed.

For the evaluation of the compression tests, the recorded load–displacement curve has been converted into a stress–strain curve. The Sneddon correction was applied to correct the displacement [60]. The real displacement $\Delta X_{\text{Pillar}}^{\text{Sneddon}}$ is calculated from the measured displacement ΔX_{total} by:

$$\Delta X_{\text{pillar}}^{\text{Sneddon}} = \Delta X_{\text{total}} - \frac{(1 - \upsilon_{\text{sub}}^2)f}{2E_{\text{sub}}R_{\text{base}}} - \frac{(1 - \upsilon_{\text{ind}}^2)f}{2E_{\text{ind}}R_{\text{top}}} \quad (1)$$

$$\varepsilon_{\text{pillar}}^{\text{Sneddon}} = \frac{\Delta X_{\text{pillar}}^{\text{Sneddon}}}{h} \quad (2)$$

where υ_{sub} and υ_{ind} represent the Poission's ratio of substrate and indenter, E_{sub} and E_{ind} for their Young's modulus and R_{top} and R_{base} for the top and base radius of the pillar. For non-tilted samples the silicon wafer is assumed as substrate with Young's modulus $E = 127$ GPa [61] and a Poisson's ratio $\upsilon = 0.221$ [62]. Tilting the pillar by 90° means the pillar consists only of coating material without substrate. The angles between 10° and 80° are something between. We therefore used a linear interpolation between these two extremes, leading to a relative deviation of less than 7% on the strain for the experiments presented here. The taper of a micropillar will lead to a deviation between the calculated and true stress states if only the top diameter is used [60]. Evaluation of the SEM images showed that the taper angle of the pillar was always below 5°, and mostly below 2°. Nevertheless, as this taper may vary slightly between pillars with differing radii, we opt to calculate an average radius R_{avg} for the pillar simply using top and base radius R_{top} and R_{base}:

$$R_{\text{avg}} = \frac{R_{\text{top}} + R_{\text{base}}}{2} \quad (3)$$

then calculating the stress, σ, in the pillar under an applied load, P, via the equation:

$$\sigma = \frac{P}{\pi R_{avg}^2} \tag{4}$$

Results

Coatings properties

The measured chemical composition of the DCMS and HPPMS grown coatings are $V_{0.49}Al_{0.51}N$ and $V_{0.47}Al_{0.53}N$, respectively. These coatings are typically slightly overstoichiometric in nitrogen content [16]. X-ray diffraction structural analysis of the coatings revealed single phase cubic structure (space group $Fm\bar{3}m$, NaCl prototype structure) for the coatings investigated in this study. Both coatings exhibit a fine-grained columnar structure, as shown in Fig. 1. However, the DCMS-grown coating is characterised by pronounced columnar grain boundaries with partially underdense regions originating from limited surface diffusion during the growth. Contrary, the higher peak power density in the HPPMS process increases the number of energetic particles arriving at the growing film surface resulting in a higher adatom surface mobility and hence, denser microstructure. This difference can also be seen in Fig. 1 where the DCMS coating shows distinct underdense boundaries (white regions along the columns in Fig. 1a) in comparison to the dense HPPMS grown coating. This difference is also reflected in the hardness and modulus values of the two coatings determined by nanoindentation (Table 1) in which the DCMS deposited sample shows reduced indentation hardness and Young's modulus by 21% and 12%, respectively, in comparison to the HPPMS grown coating.

Size and strain rate effects

Tests performed to establish reliable experimental parameters showed that the fracture stress and strain hardly changed despite varying load rates. The fracture parameters over the load rate are shown in Fig. 2a and b for pillars with 0° tilt. Similar evaluations on micropillars with different diameters show that the failure stress in a range of 0.75–1.0 μm was constant, as shown in Fig. 2c and d. Furthermore, SEM images showed that the 1.25 μm diameter pillars were completely delaminated in some cases (Fig. 3).

Compression of micropillars tilted to column growth direction

Representative stress–strain curves are plotted against the tilt angle in Fig. 4 for both coatings. From these curves, the fracture stresses and strains are determined and plotted against the tilt angle, later shown in Fig. 7. From SE micrographs after the experiment, three types of fracture behaviour can be identified, shown for DCMS micropillars in Fig. 5. Samples from HPPMS exhibited similar behaviour. A brittle fracture of the pillar is observed in the range of 0°–20°, where single or several connected columns are extracted (Fig. 5a, d). In the range of 30°–60°, a sliding of the columns along their boundaries is observed (Fig. 5b, e). At higher tilt angles of 70°–90°, the pillars fail along the column boundaries (Fig. 5c, f). In order to better distinguish the three regimes, they are shown in different colours in Figs. 4 and 5 and the same colour scheme for those regimes is used for all figures in the following.

TABLE 1: Coating properties determined by STEM (thickness), X-ray analysis (residual stress), and nanoindentation (hardness and modulus).

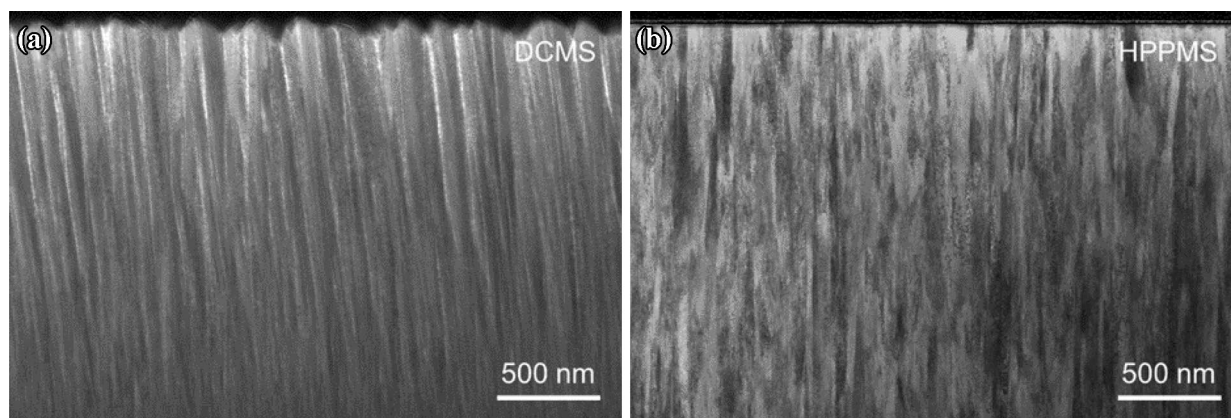| Parameter	Unit	DCMS	HPPMS
Coating thickness	μm	3.0	2.7
Residual stress	GPa	-0.9 ± 0.3	-3.2 ± 0.4
Indentation hardness	GPa	25.8 ± 1.4	31.1 ± 0.9
Young's modulus	GPa	380 ± 20	426 ± 13

Figure 1: Bright field STEM micrographs of cross-section of (a) DCMS and (b) HPPMS coatings on silicon wafer.
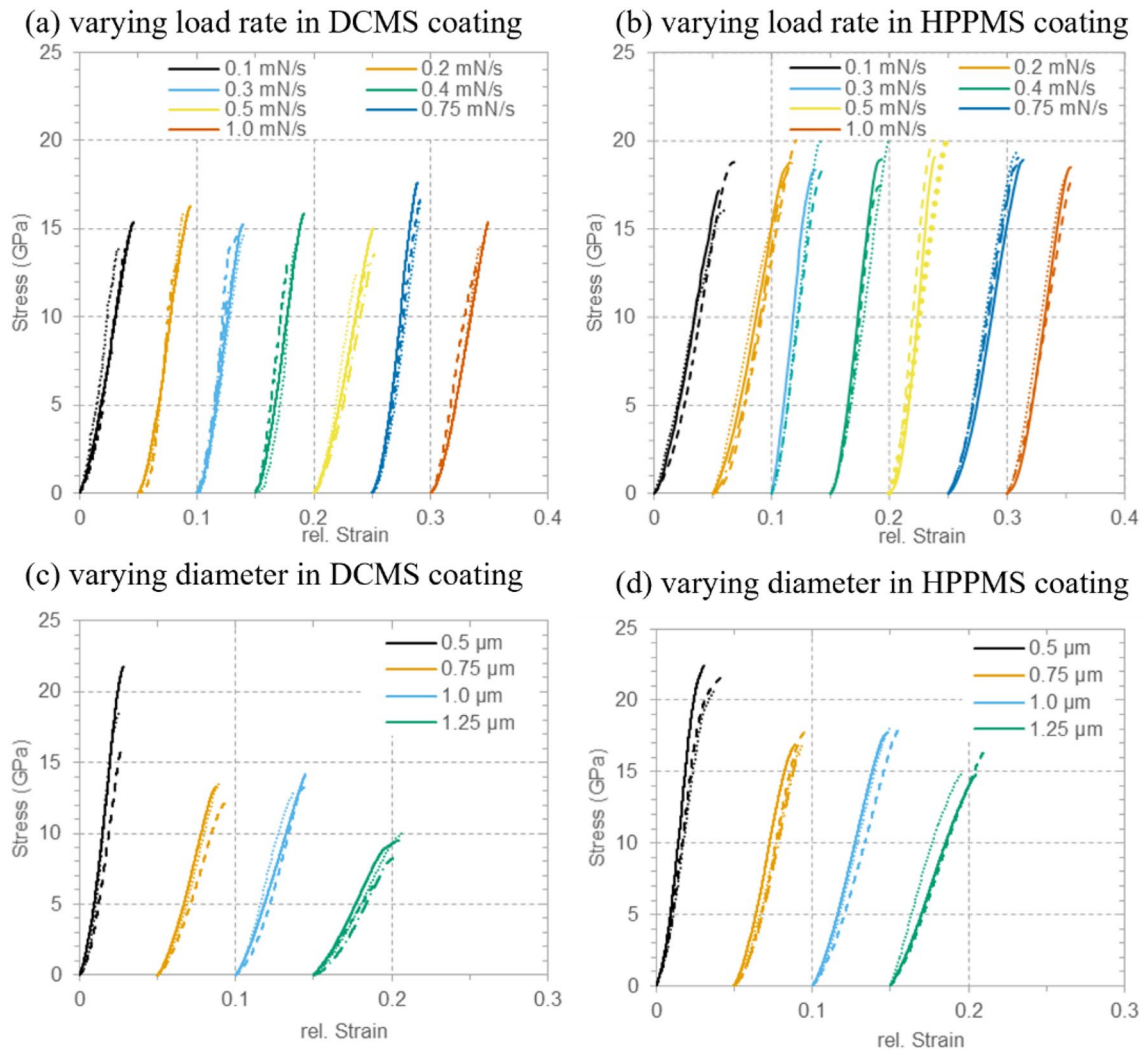
Figure 2: Stress–strain curves for varying load rate and pillar diameter in DCMS and HPPMS coatings for pillars with 0° tilt. Three representative curves are plotted for each experimental condition.
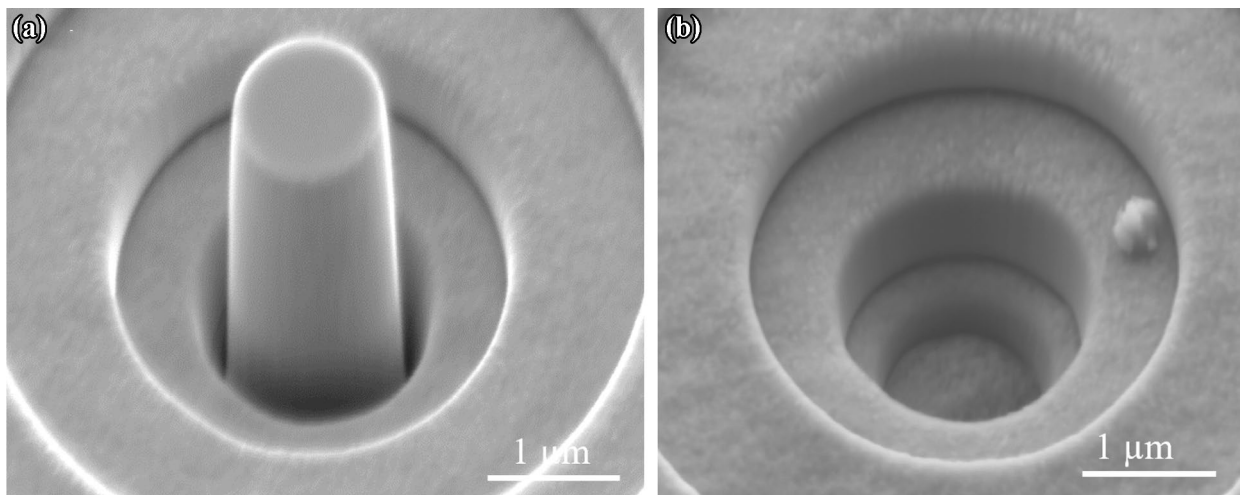

Figure 3: Micropillar with 1.25 μm diameter in DCMS-grown coating (a) before and (b) after compression test when delamination was observed.
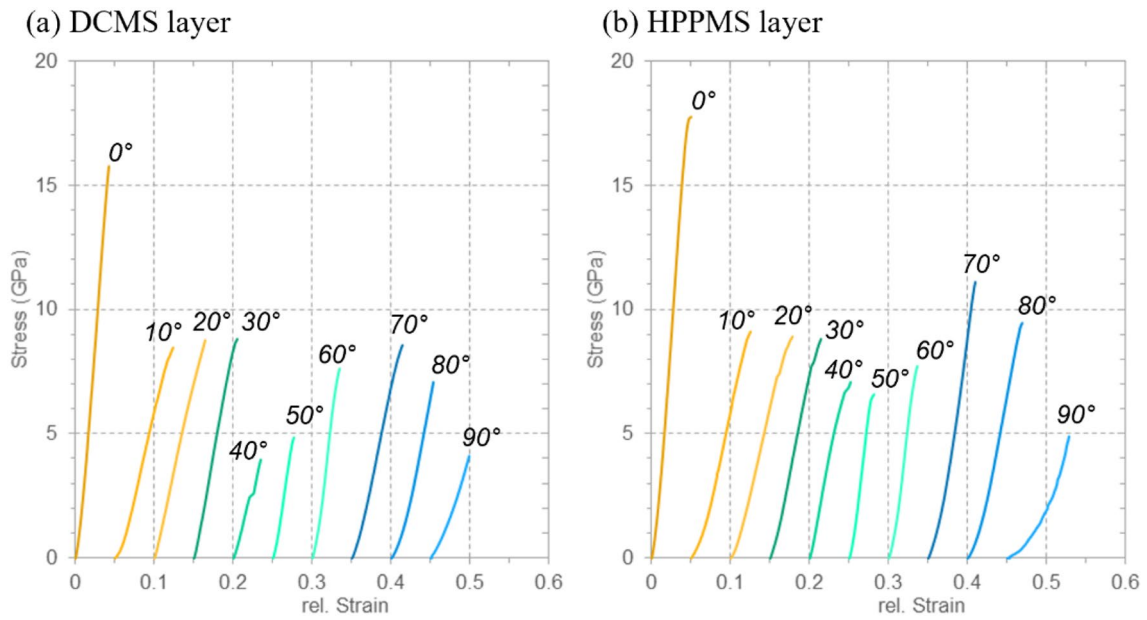
(a) DCMS layer

(b) HPPMS layer

Figure 4: Resulting stress–strain curves over the tilt angle in (a) DCMS coating and (b) HPPMS coating.
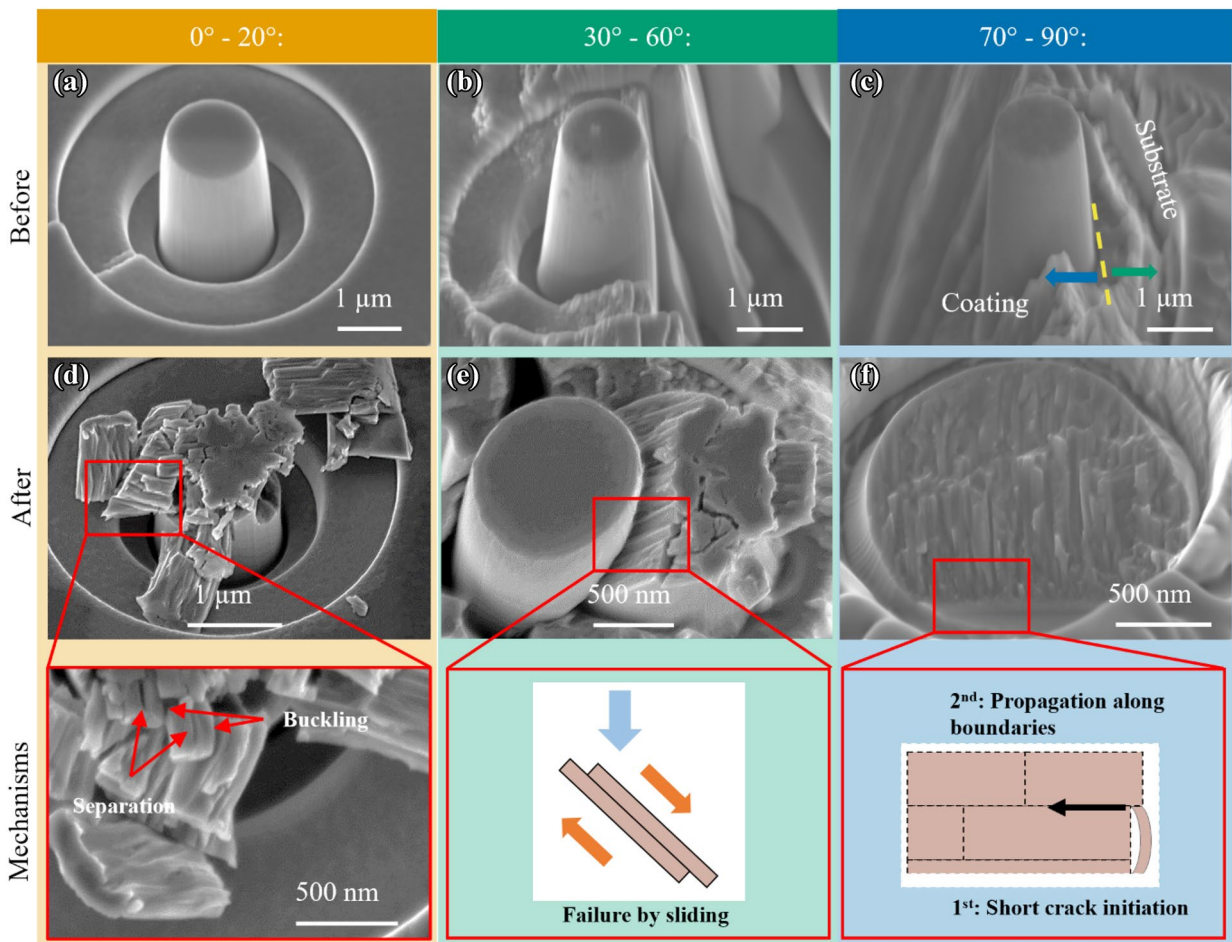

Figure 5: SE micrographs of micropillars in the DCMS sample, manufactured at 0°, 30°, and 90° to the growth direction of the coating (a)–(c) before and (d)–(f) after compression with exemplary highlighting observed mechanisms.

Discussion

In the course of this section, the possible failure mechanisms are identified from the SEM imaging observations and the critical stresses are described quantitatively using commonly known equations. These are then compared with the experimentally determined failure stresses. Finally, we compare the results presented and discussed here with those from other test methods applied in the literature.

Determination of fracture mechanisms

Buckling

When looking at the remains of the micropillars in the range of 0°–20° (Fig. 5a, d) after deformation, it is observed that some columns no longer run straight and are curved. This suggests buckling [63]. Since (V,Al)N is also a brittle material [30], it is assumed that it is initially a purely elastic Euler buckling. The elastic Euler force P^* in the micropillar can be determined using the Euler equation [63, 64].

$$P^* = \left(\frac{\pi}{L_b}\right)^2 EI \tag{5}$$

In (Eq. 5), the product from Young's Modulus and second momentum of area EI represents the resistance to bending of the micropillar and L_b the curved length, depending on the actual length of the micropillar and the boundary conditions. If a bending beam is fixed on both sides or on one side, the length L_b can be equated with the current length of this bending beam. The second moment of area I is only depending on the sample radius R and can be written as:

$$I = \frac{\pi}{4} R^4 \tag{6}$$

Normally, the elastic force required for buckling in a micropillar is significantly higher than the force actually achieved, nevertheless, it was found in Si micropillars that a small change in aspect ratio could lead to Euler buckling [63]. For an average micropillar in this test series with a pillar radius of $R_{\text{Pillar}} = 487 \pm 11$ nm and a length of $L_{\text{Pillar}} = 2038 \pm 235$ nm, as well as a Young's modulus of $E = 426 \pm 13$ GPa, the elastic buckling force is calculated to be $P^* = 45 \pm 3$ mN. In relation to the top area of the micropillar, as the maximum stress in the pillar, this equates to a Euler buckling stress of $\sigma^* = 60 \pm 5$ GPa. A stress of this magnitude has never been observed here at any time and the micropillars fail at $\leq 25\%$ of this stress.

However, the post-mortem SEM images suggest that separation and, therefore, independent deformation of the columns inside each pillar may be possible. Looking then at a single column, a different picture emerges. As measured from STEM images (Fig. 1), an average column has a length $L_{\text{Column}} = 460 \pm 40$ nm and a radius of $R_{\text{Column}} = 60 \pm 10$ nm. Calculated from this an elastic buckling force of $P^* = 0.16 \pm 0.07$ mN and thus an elastic buckling stress of $\sigma^* = 16.0 \pm 4.9$ GPa is needed for Euler buckling. Applied stresses on a single column of this magnitude can be observed up to a tilt angle of about 70°, but the stress acting exactly along the column decreases with increasing tilt angle, so that the separation of columns or sliding becomes more preferable and buckling is only observed at lower tilt angles. However, since the columns are not uniform, individual particularly long and thin columns can also reach the elastic buckling stress up to a tilt angle of about 30°. Due to the l^{-2} and r^4 dependence of the buckling stress on column dimensions, only small deviations from the mean are needed for a column to buckle; it is sufficient if the column is only one standard deviation away from the mean value to reduce the elastic buckling stress from ~ 16 to ~ 11 GPa.

Separation of columns

Deflection of these columns during buckling leads to tensile stresses on the column boundaries which supports the separation of these columns from their surrounding columns. Consequently, the adhesion between the columns must be overcome. The stress required for this will be related to the driving force given by the difference between the energy stored in the elastic deformation U_{el} that is released and the energy used to create the new surfaces U_{ad} [65].

$$U_{el} = \frac{\sigma^2}{2E} l_0 A \tag{7}$$

$$U_{ad} = 2\gamma A \tag{8}$$

$$\sigma_{cr} = \frac{\partial U_{\text{total}}}{\partial A} = \frac{\partial (U_{ad} - U_{el})}{\partial A} = 0 \tag{9}$$

where σ is the applied stress, E the Young's Modulus, A the contact area, γ the surface energy and l_0 is the dimension in the normal direction to the contact area. To simplify, in this model we assume a mean column diameter as l_0 and the projected cross-sectional area of a column as the contact area. Combining (Eq. 7) and (Eq. 8) with (Eq. 9) under these conditions leads to an expression for the critical adhesion stress.

$$\sigma_{\text{cr,adh}} = \sqrt{\frac{4E\gamma}{l_0}} \tag{10}$$

If the energy expended is less than that released, the adhesion can be overcome, and the columns can separate spontaneously. With the same column radius as above for the critical length l_0 and a surface energy of $\gamma = 1.8 \pm 0.9$ J/m^2 [66], the

critical stress for a spontaneous separation of the columns is calculated as σ_{cr} = 5.4 ± 1.4 GPa.

In the real case, the contact area would be much larger and a separation of the considered column not only from the neighbouring column but from all surrounding columns would have to occur. Our model therefore overestimates the required elastic energy (Eq. 7). However, it also underestimates the energy to generate the new surfaces (Eq. 8), as these new surfaces are created along the column boundaries with a lower atomic bonding density compared to the bulk material used to calculate the surface energy used here. Also, in the DCMS coatings the grain boundaries are underdense compared to HPPMS coatings.

Since our model agrees to a large extent with the experimentally determined fracture stresses, we assume that these effects approximately compensate each other. A numerical model that quantifies these effects is therefore not part of this work.

Micro-cracking

The bending of the columns by buckling further leads to a tensile stress along the columns, so that micro-cracks can form. The tensile stress required to form micro-cracks can be determined using the Griffith criterion [67, 68]:

$$\sigma_{cr,crack} \geq \sqrt{\frac{2\gamma E}{\pi a_{cr}}} \qquad (11)$$

where E is the Young's Modulus, γ the surface energy and a_{cr} the critical crack length. Assuming half the diameter of a column for the critical crack length a_{cr}, the required tangential stress $\sigma_{cr,crack}$ = 3.1 ± 1.1 GPa is obtained.

The effects of column separation and micro-cracking caused by buckling are shown schematically in Fig. 6a and b. Here the observed behaviour is described by considering a randomly aligned column in the micropillar as an example. The stress acting on the micropillar can be divided into a stress perpendicular to the column and a stress parallel to the column. Euler buckling can only occur if the stress parallel to the column is higher than the elastic buckling stress of σ^* = 16.0 ± 4.9 GPa. A schematic sketch of a column and the parallel and vertical acting stress are shown in Fig. 6c. The perpendicular stress, on the other hand, counteracts the tensile stress induced by the buckling at small tilting angles and thus increases the stress required to overcome the adhesion.

At higher tilt angles, the effect of the parallel stresses is inducing a shear stress and working against the buckling, while the perpendicular stresses now are nearly the same as the applied stress, leading to the cracking/separation. It can be seen in Fig. 6d that it is hard to reach the critical stress for an average column. Consequently, the failure has to start at certain inhomogeneities as will be described later.

Sliding

At intermediate angles, 30°–60°, the columns have slipped against each other, as can be seen in Fig. 5e. Although no plasticity is visible in the stress–strain curves, we can analogously use Schmid's law to describe this behaviour:

$$\tau_{CRSS} = \sigma_y \cos(\lambda)\cos(\kappa) \qquad (12)$$

where λ is the angle between column growth direction and load direction and κ is the normal direction to the columns. The critical shear stress to activate column slip can be assumed to occur when the yield point is reached. We use a modulus-dependent factor from Vandeperre et al. [69] to estimate the yield stress based upon the hardness, H, as follows using an average ratio of H/E of 0.07 (0.067 for DCMS and 0.073 for HPPMS) from Table 1:

$$\sigma_Y = 0.31 \times H \qquad (13)$$

This leads to an expected yield point of σ_Y = 8.0 GPa and σ_Y = 9.6 GPa in DCMS and HPPMS grown coatings, respectively. Using Eq. (11), the critical shear stress can be subsequently calculated as τ_{CRSS} = 3.9 GPa and τ_{CRSS} = 4.3 GPa for DCMS and HPPMS grown coatings at 45°, respectively. Compared with the shear stresses, τ_{RSS} which were calculated using equation (Eq. 12) from the stresses measured during the test (see Fig. 7a, b), it can be seen that the measured shear stresses are broadly close in both layers for the range of 30°–60°.

Short cracks at the bottom

At tilt angles between 70° and 90°, as can be seen in Fig. 5f, crack propagation and subsequent failure occurs mainly perpendicular to the loading direction. The crack initiation occurs at microstructural inhomogeneities which are present near the coating substrate interface and then spread via micro-cracks along the column boundaries. This is schematically shown in Fig. 6d. A similar behaviour of micro-cracks has been observed before [70–75]. These studies have shown that microstructurally short cracks have an abnormal propagation behaviour compared to the long cracks, which are well described.

An attempt to explain the abnormal behaviour is given by studies on the fracture behaviour of ceramic nanocomposites by Veprek et al. [73]. They have shown that the Griffith criterion also applies to such nano-cracks, but the stress intensity factors are many times higher (up to 140 times), since the crack length can only be a fraction of the crystallite size and the smallest radius of the crack tip corresponds only to the interatomic distance. Ovid'ko [75] used this approach to explain the initiation of nano-cracks by a movement and concentration of grain boundary dislocations to triple points. Accordingly, a nano-crack occurs at the triple point when its Burgers vector exceeds the critical value of the equilibrium length. A theoretical model [74] for numerical analysis of the equilibrium length
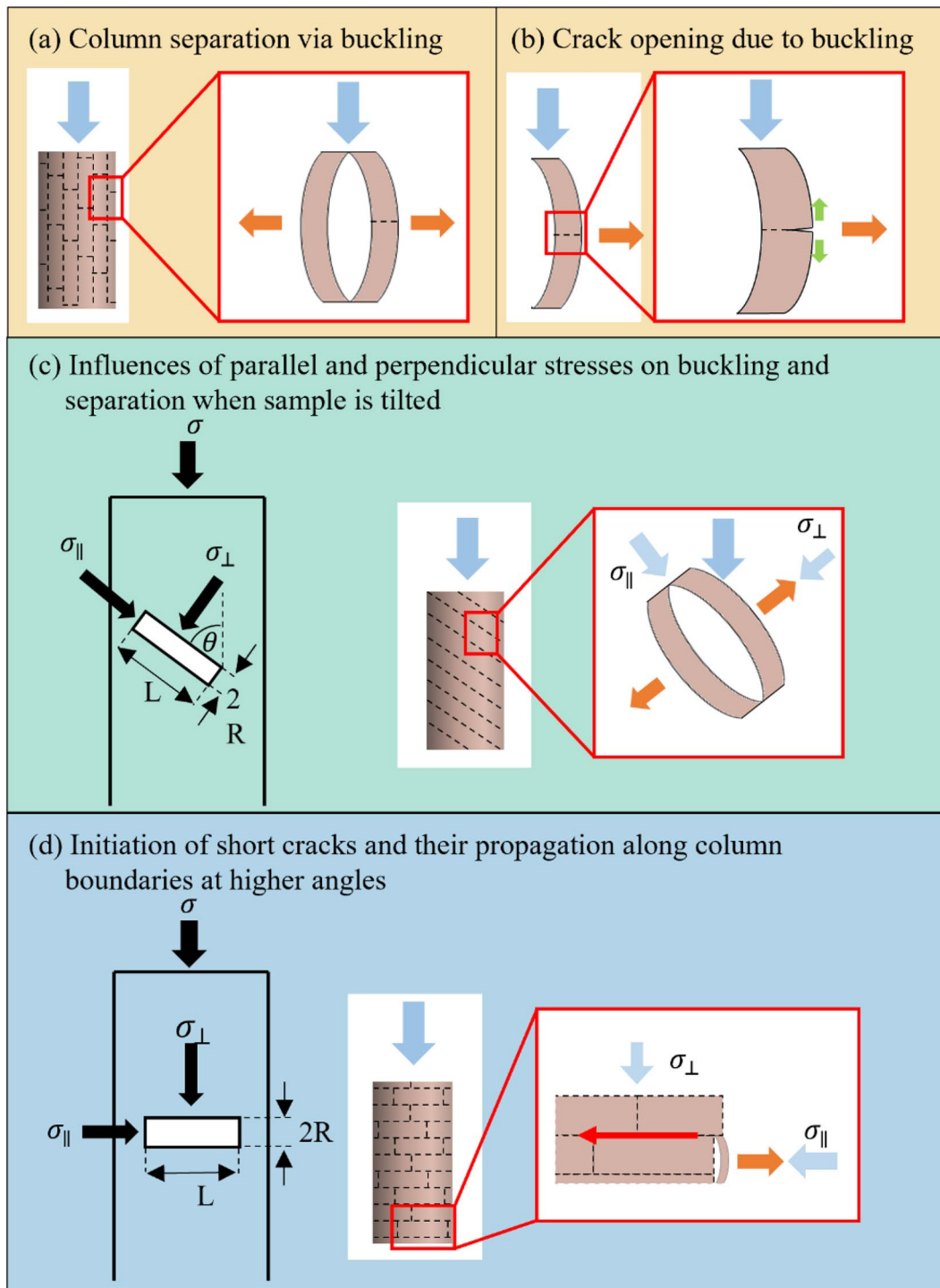
Figure 6: Schematic drawing of (a) introducing tensile stress by buckling, (b) micro-crack opening, (c) and (d) crack initiation at inhomogeneity and possible crack path.

and stress tensor shows good agreement with in situ experiments on nickel. For the experiments carried out here, high-resolution in situ experiments would be necessary to obtain the corresponding input data.

Combining fracture mechanisms and fracture behaviour

If the fracture stress measured by micropillar compression is compared with the stress that is calculated via equations (5, 10,
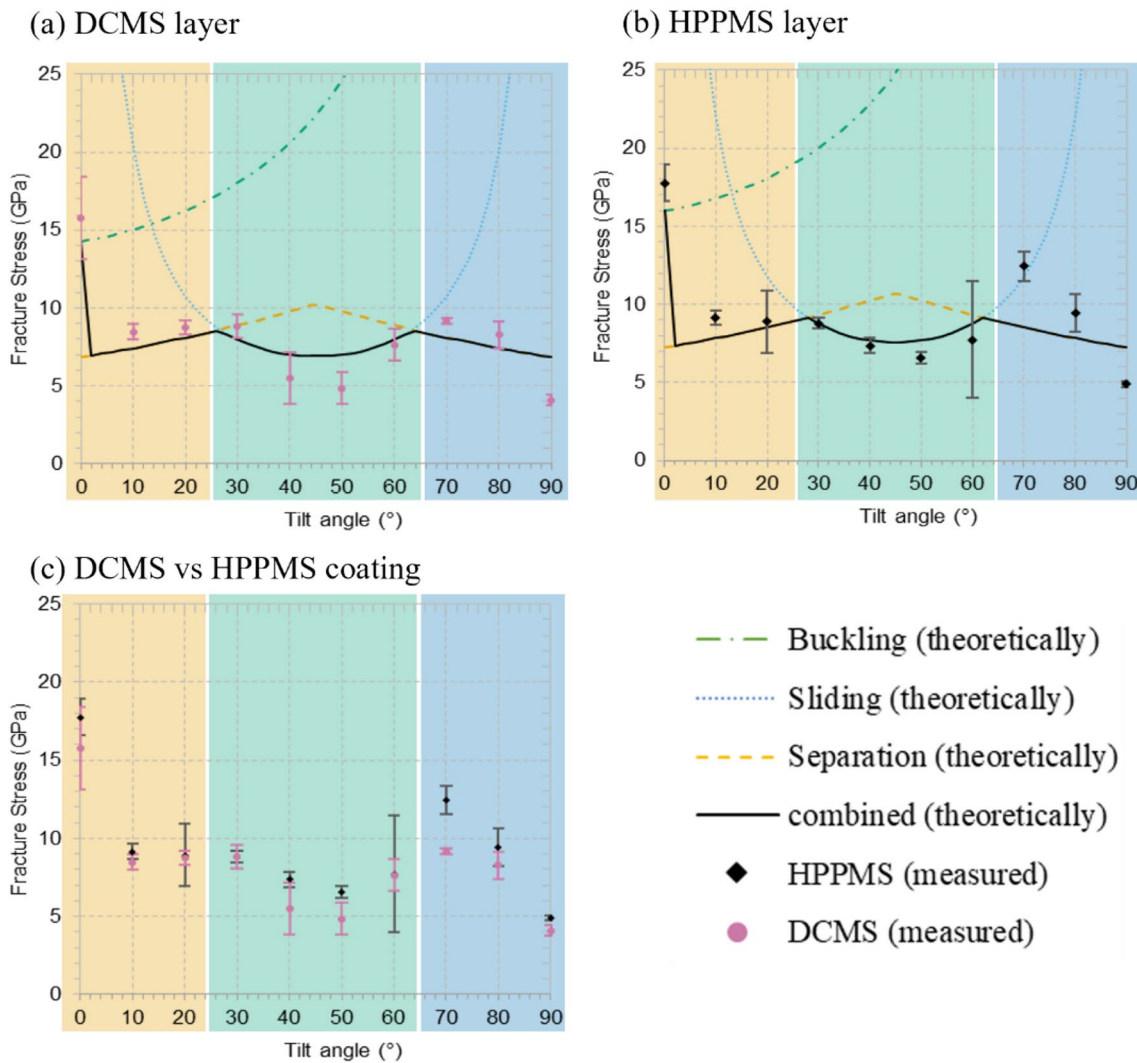
(a) DCMS layer

(b) HPPMS layer

(c) DCMS vs HPPMS coating

- — · — Buckling (theoretically)
- ········ Sliding (theoretically)
- – – – Separation (theoretically)
- —— combined (theoretically)
- ◆ HPPMS (measured)
- ● DCMS (measured)

Figure 7: Measured fracture stresses compared to calculated critical stresses in (a) DCMS and (b) HPPMS in the three regions where buckling, sliding or separation was found and the expected behaviour by combining all mechanisms and (c) comparing fracture stresses in DCMS and HPPMS coatings.

11 and 13) to reach the critical stresses of the active fracture mechanisms as shown in Fig. 7a and b, it is found that they are largely identical to the mechanism with the lowest critical stress.

Despite densification in case of using the HPPMS process when comparing the measured fracture stresses of HPPMS and DCMS deposited layers (Fig. 7c), a widely similar behaviour for DCMS and HPPMS is observed.

For non-tilted micropillars (0°), where buckling is the initiating mechanism, a high fracture stress for both DCMS and HPPMS layers is measured. Due to the densification in the HPPMS grown layer, a higher fracture stress is expected. However, as observed in Fig. 7, the difference is not resolvable due to the scattering of the fracture stress data for the DCMS layer. In the range between 10° and up to 20°, where separation is the dominant mechanism, there is no significant difference between the two layers. In contrast, for tilt angles of 40° and 50° where

sliding is clearly dominant, a small difference in fracture properties between the two layers is observed. This could be interpreted as the denser interfaces in the case of HPPMS deposited layer led to a higher resistance to sliding (shear loading of the interface), but do not affect the resistance to separation (tensile loading of the interface). At tilt angles of 30° and 60° we observe a transition area where a combination of both, sliding and separation, are the dominating mechanisms. Also, in this area, the experimental data did not show a difference between HPPMS and DCMS-grown layers. In the range from 70° and higher angles, where failure begins at small microstructural inhomogeneities, some differences in fracture behaviour can be seen. However, in the absence of a specific description of the initiation and propagation of the short cracks responsible for failure initiation, it is difficult to say whether a difference should be expected. In general, in both coatings the growth starts with a stage where

the columns are not well developed (coalescence of islands). However, according to the explanation given by Ovid'ko [75], it could be assumed that in the growth region of coalescence of islands the movement and concentration of grain boundary dislocations to triple points is activated at lower stress levels in DCMS layers.

Comparison to beam bending, indentation and scratch tests

Comparing the fracture behaviour from micropillar compression and previously performed beam bending tests in tensile stress (Mode I) a similar behaviour can be seen. In beam bending Mode I the measured fracture stresses of $\sigma = 5.5 \pm 0.3$ GPa in (V,Al)N [44] is well fitting to the one calculated for column separation ($\sigma_{cr} = 5.4 \pm 1.4$ GPa) on non-tilted micropillars and is close to the measured fracture stresses (6.8 ± 1.6 GPa for DCMS and 7.2 ± 1.2 GPa for HPPMS grown coatings). However, the actual fracture stress in non-tilted micropillars is much higher since the required tensile stress is applied by buckling. Therefore, at first the critical buckling stress of the columns must be overcome.

The observed fracture behaviour consisting of buckling, separation of columns and micro-cracks has also been observed in (Cr,Al)N-layers in previous nano-scratch tests [52, 70], where a combination from compressive and lateral stress is applied. This stress state is very similar to the application case. It was found that the coating cracking behaviour is dominated by separation of columns, micro-cracks and a plastic deformation of single columns [50]. Hence, the stress state and the cracking behaviour in the scratch test appeared to be a combination of the behaviour observed in non-tilted micropillar (0°) and 90° tilted to the column growth direction during this work.

Thus, by means of orientation-dependent micropillar compression we are able to separately investigate comparable stresses to beam bending on the one hand, and, on the other hand, the same mechanisms as in the close-to-application-case tests, like nano-scratch or Rockwell impact tests.

The here discussed test methods, which were applied to investigate TMN coatings before, can be divided based upon their time (and cost) consumption and the possibility to observe individual mechanisms. As schematically shown in Fig. 8, it is naturally of interest therefore to find a technique by which mechanisms can be observed separately with low preparation and investigation time. We show here that micropillar compression is in fact a suitable and efficient method even for these highly anisotropic coatings. Compared to cantilever bending methods, micropillar preparation takes less than half the cutting time in FIB with about 10–15 min per pillar and tested under much simpler experimental conditions, in particular also ex situ, as technical stress and strain can
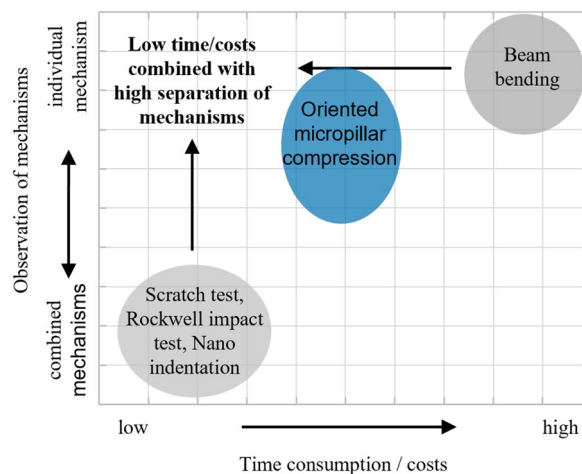

Figure 8: Overview and classification by time/cost consumption and the ability of micro-mechanical testing methods to investigate individual deformation mechanisms.

be calculated by imaging the pillar prior deformation. This means that we regularly can perform those tests in ambient atmosphere using an optical microscope to find each experimental side. But by this we cannot see the deformation of the pillars during the experiment. Only if this is required we can perform the micropillar compression in situ in SEM, whereas for beam bending all experiments take place inside SEM in order to measure the exact position of the tip and ensure its central placement along the beam. Naturally, this type of experiment needs more resources and time to perform while the measured fracture stresses and other failure properties appear to be comparable.

Another advantage of micropillar compression is the possibility to test under different directions to the growth direction, which would in case of beam bending require much thicker coatings than usually applied. A 10 μm long beam with a cross-section area of 1×1 μm² in 45°-orientation to the growth direction would need a coating thickness around 11 μm, which is more than three times higher than the coating thicknesses used here and means more than three times higher deposition time. Furthermore, the increased coating thickness is supposed to lower the density and increase the roughness of the coating [18] which maybe affect the mechanical properties.

Conclusions

Two series of (V,Al)N-layers were deposited by DCMS and HPPMS processes, both with a columnar microstructure. They were compared with respect to their fracture behaviour using micropillar compression at different angles between the growth
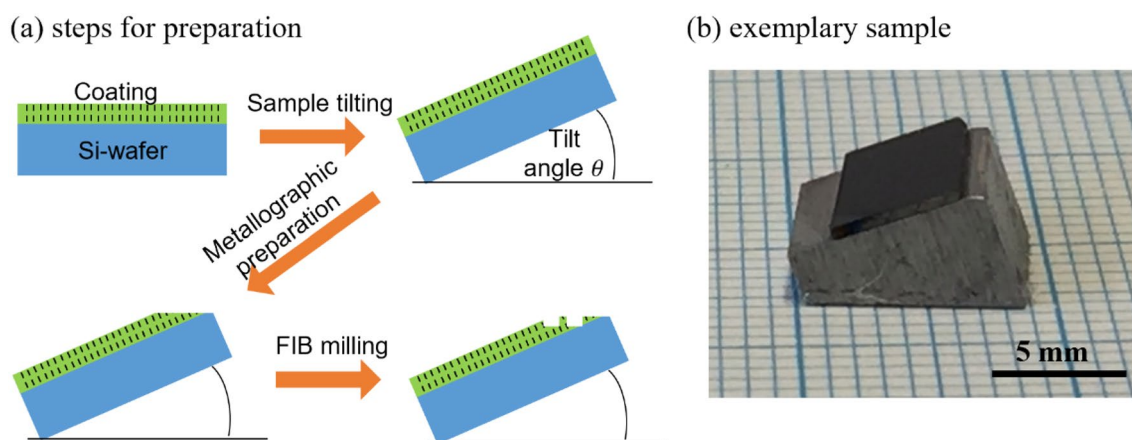
(a) steps for preparation

(b) exemplary sample

Figure 9: (a)Schematic drawing of steps in sample preparation for micropillars tilted with respect to the growth/column direction and (b) exemplary sample before polishing.

and compression directions. It was shown that depending on the grain alignment different fracture mechanisms such as buckling, column separation, sliding and micro-cracks were activated. The comparison with nano-scratch test shows that the non-tilted micropillars are closest to the application case; however, in the micropillar compression test, the individual fracture mechanisms could be observed separately and related to simple models of the underlying mechanism. Thus, it was possible to determine the critical stresses to activate these mechanisms, which will allow a description of the deformation behaviour of these hard coatings in predictive models. Furthermore, the experiments will be extended to Transition Metal Oxynitrides to investigate the effect of chemistry and to include this effect to describe and predict the fracture properties of a wider range of hard coatings.

Comparing DCMS and HPPMS coatings, it was shown that the characteristics of the two coating processes do not significantly influence the fracture properties and behaviour as long as the resulting coatings have similar columnar microstructures. While there is a densification in HPPMS coatings and some differences were measured for this layer at specific tilt angles, no significant difference with respect to fracture properties was observed between the coatings grown by DCMS and HPPMS. Dedicated shear tests and high-resolution microscopy on the boundary structures may help to resolve the fracture behaviour differences of these coatings in future studies.

Methodology

For the production of micropillars with differently aligned columns, the coated silicon wafers were glued onto pre-tilted holders and prepared metallographically by polishing with diamond suspension (1–0.25 μm particle size). The further production was then carried out with a focussed ion beam in a scanning electron microscope (SEM) (Helios NanoLab 600i from FEI, NL). The process of milling consisted of six steps with beam currents between 9.1 nA and 80 pA. Figure 9 shows a schematic representation of the preparation steps.

Author contributions

Text and mechanical testing: MRS. Coating deposition and determination of chemical composition, microstructure and mechanical properties (sections 'Coatings and deposition' and 'Coatings properties' also Fig. 1 and Table 1): SKA. Supervision and review of experiments and manuscript: JSK-LG, MH, JMS, and SK-K.

Data availability

The datasets generated during and analysed during the current study are available from the corresponding author on reasonable request.

Code availability

Not applicable.

Declarations

Conflict of interest Not applicable.

Open Access

References

1. H. Rueß, D. Music, A. Bahr, J.M. Schneider, Effect of chemical composition, defect structure, and stress state on the elastic properties of $(V_{1-x}Al_x)_{1-y}N_y$. J. Phys.: Condens. Matter **32**, 025901 (2020)

2. P.H. Mayrhofer, H. Willmann, A.E. Reiter, Structure and phase evolution of Cr–Al–N coatings during annealing. Surf. Coat. Technol. **202**, 4935–4938 (2008)

3. P.H. Mayrhofer, D. Music, J.M. Schneider, Influence of the Al distribution on the structure, elastic properties, and phase stability of supersaturated $Ti_{1-x}Al_xN$. J. Appl. Phys. **100**(9), 094906 (2006)

4. M. Berger, M. Larsson, S. Hogmark, Evaluation of magnetron-sputtered TiB_2 intended for tribological applications. Surf. Coat. Technol. **124**(2–3), 253–261 (2000)

5. A. Hörling, L. Hultman, M. Odén, J. Sjölén, L. Karlsson, Mechanical properties and machining performance of $Ti_{1-x}Al_xN$-coated cutting tools. Surf. Coat. Technol. **191**, 384–392 (2005)

6. W.S. Williams, High-temperature thermal conductivity of transition metal carbides and nitrides. J. Am. Ceram. Soc. **49**(3), 156–159 (1966)

7. R. Rachbauer, J.J. Gengler, A.A. Voevodin, K. Resch, P.H. Mayrhofer, Temperature driven evolution of thermal, electrical, and optical properties of Ti–Al–N coatings. Acta Mater. **60**(5), 2091–2096 (2012)

8. A.D. McLeod, J.S. Haggerty, D.R. Sadoway, Electrical resistivities of monocrystalline and polycrystalline TiB_2. J. Am. Ceram. Soc. **67**(11), 705–708 (1984)

9. K. Bobzin, G. Grundmeier, T. Brögelmann, T. de los Arcos, M. Wiesing, N.C. Kruppe, Nitridische und oxinitridische HPPMS-Beschichtungen für den Einsatz in der Kunststoffverarbeitung (Teil 2). Vakuum in Forschung und Praxis **29**(1), 24–28 (2017)

10. K. Bobzin, G. Grundmeier, T. Brögelmann, T. de los Arcos, M. Wiesing, N.C. Kruppe, Nitridische und oxinitridische HPPMS-Beschichtungen für den Einsatz in der Kunststoffverarbeitung (Teil 1). Vakuum in Forschung und Praxis **28**(6), 28–33 (2016)

11. K. Bobzin, N. Bagcivan, M. Ewering, Hartstoffschichten der Zukunft—Oxidische Schichten und HPPMS-Schichten für anspruchsvolle Zerspanaufgaben. Dünne Schichten **22**(6), 31–35 (2010)

12. E. Lugscheider, K. Bobzin, Th. Hornig, M. Maes, Investigation of the residual stresses and mechanical properties of (Cr,Al)N arc PVD coatings used for semi-solid metal (SSM) forming dies. Thin Solid Films **420–421**, 318–323 (2002)

13. V. Kouznetsov, K. Maca, J.M. Schneider, U. Helmersson, I. Petrov, A novel pulsed magnetron sputter technique utilizing very high target power densities. Surf. Coat. Technol. **122**, 290–293 (1999)

14. K. Macák, V. Kouznetsov, J.M. Schneider, U. Helmersson, I. Petrov, Ionized sputter deposition using an extremely high plasma density pulsed magnetron discharge. J. Vac. Sci. Technol. A **18**(1533), 1533–1537 (2000)

15. A.P. Ehiasarian, R. New, W.-D. Münz, L. Hultman, U. Helmersson, V. Kouznetsov, Influence of high power densities on the composition of pulsed magnetron plasmas. Vacuum **65**(2), 147–154 (2002)

16. G. Greczynski, S. Mráz, M. Hans, D. Primetzhofer, J. Lu, L. Hultman, J.M. Schneider, Unprecedented Al supersaturation in singlephase rock salt structure VAlN films by Al+ subplantation. J. Appl. Phys. **121**, 171907 (2017)

17. M. Samuelsson, D. Lundin, J. Jensen, M.A. Raadu, J.T. Gudmundsson, U. Helmersson, On the film density using high power impulse magnetron sputtering. Surf. Coat. Technol. **205**, 591–596 (2021)

18. H. Hajihoseini, J.T. Gudmundsson, Vanadium and vanadium nitride thin films grown by high power impulse magnetron sputtering. J. Phys. D **50**, 505302 (2017)

19. S. Karimi Aghda, D. Music, Y. Unutulmazsoy, H. Han Sua, S. Mráz, M. Hans, D. Primetzhofer, A. Anders, J.M. Schneider, Unravelling the ion-energy-dependent structure evolution and its implications for the elastic properties of (V,Al)N thin films. Acta Mater. **214**, 117003 (2021)

20. G.M. Pharr, W.C. Oliver, Measurement of thin film mechanical properties using nanoindentation. MRS Bull. **17**, 28–33 (1992)

21. W.C. Oliver, G.M. Pharr, An improved technique for determining hardness and elastic modulus using load and displacement sensing indentation experiments. J. Mater. Res. **7**(6), 1564–1583 (1992)

22. S.J. Bull, Nanoindentation of coatings. J. Appl. Phys. **38**(R393), 393–413 (2005)

23. S.V. Hainsworth, H.W. Chandler, T.F. Page, Analysis of nanoindentation load-displacement loading curves. J. Mater. Res. Lett. **11**(8), 1987–1995 (1996)

24. H.N. Mathur, V. Maier-Kiener, S. Korte-Kerzel, Deformation in the g-$Mg_{17}Al_{12}$ phase at 25–278°C. Acta Mater. **113**, 221–229 (2016)

25. A.E. Reiter, V.H. Derflinger, B. Hanselmann, T. Bachmann, B. Sartory, Investigation of the properties of $Al_{1-x}Cr_xN$ coatings prepared by cathodic arc evaporation. Surf. Coat. Technol. **200**, 2114–2122 (2005)

26. J.-E. Sundgren, Structure and properties of TiN coatings. Thin Solid Films **128**(1–2), 21–44 (1985)

27. M. Hans, M. to Baben, D. Music, J. Ebenhöch, D. Primetzhofer, D. Kurapov, M. Arndt, H. Rudigier, J.M. Schneider, Effect of oxygen incorporation on the structure and elasticity of Ti–Al–O–N coatings synthesized by cathodic arc and high power pulsed magnetron sputtering. J. Appl. Phys. **116**, 093515 (2014)

28. K.P. Shaha, H. Rueβ, S.J. Rotert, M. to Baben, D. Music, J.M. Schneider, Nonmetal sublattice population induced defect structure in transition metal aluminum oxynitrides. Appl. Phys. Lett. **103**, 221905 (2013)

29. F. Giuliani, C. Ciurea, V. Bhakhri, M. Werchota, L.J. Vandeperre, P.H. Mayrhofer, Deformation behaviour of TiN and Ti–Al–N coatings at 295 to 573 K. Thin Solid Films **688**, 137363 (2019)

30. F. Jose, R. Ramaseshan, S. Dash, S. Rajagopalan, A.K. Tyagi, Significance of aluminum on hardness of titanium aluminum nitride deposited by magnetron co-sputtering. Int. J. Ceram. Technol. **6**(2), 243–248 (2009)

31. L. Zhou, D. Holec, P.H. Mayrhofer, First-principles study of elastic properties of cubic $Cr_{1-x}Al_xN$ alloys. Appl. Phys. Lett. **113**, 043511 (2013)

32. J. Musil, M. Jirout, Toughness of hard nanostructured ceramic thin films. Surf. Coat. Technol. **201**, 5148–5152 (2007)

33. J. Malzbender, G. de With, Energy dissipation, fracture toughness and the indentation load-displacement curve of coated materials. Surf. Coat. Technol. **135**, 60–68 (2000)

34. R. Soler, S. Gleich, C. Kirchlechner, C. Scheu, J.M. Schneider, G. Dehm, Fracture toughness of Mo_2BC thin films: intrinsic toughness versus system toughening. Mater. Des. **154**, 20–27 (2018)

35. S. Wurster, C. Motz, R. Pippan, Notched-Cantilever testing on the micrometer scale—effects of constraints on plasticity and fracture behaviour. In Proceedings of the 18th European Conference on Fracture (2010)

36. D. DiMaio, S.G. Roberts, Measuring fracture toughness of coatings using focused-ion-beam-machined microbeams. J. Mater. Res. **20**(2), 299–302 (2004)

37. C. Bohnert, N.J. Schmitt, S.M. Weygand, O. Kraft, R. Schwaiger, Fracture toughness characterization of single-crystalline tungsten using notched micro-cantilever specimens. Int. J. Plast. **81**, 1–17 (2016)

38. F. Iqbal, J. Ast, M. Göken, K. Durst, In situ micro-cantilever tests to study fracture properties of NiAl single crystals. Acta Mater. **60**, 1193–1200 (2012)

39. A.K. Saxena, S. Brinckmann, B. Völker, G. Dehm, C. Kirchlechner, Experimental conditions affecting the measured fracture toughness at the microscale: Notch geometry and crack extension measurement. Mater. Des. **191**, 108582 (2020)

40. J. Ast, B. Merle, K. Durst, M. Göken, Fracture toughness evaluation of NiAl single crystals by microcantilevers—a new continuous J-integral method. J. Mater. Res. **31**(23), 3786–3794 (2016)

41. M. Alfreider, D. Kozic, O. Kolednik, D. Kiener, In-situ elastic-plastic fracture mechanics on the microscale by means of continuous dynamical testing. Mater. Des. **148**, 177–187 (2018)

42. K. Matoy, H. Schönherr, T. Detzel, T. Schöberl, R. Pippan, C. Motz, G. Dehm, A comparative micro-cantilever study of the mechanical behavior of silicon based passivation films. Thin Solid Films **518**, 247–256 (2009)

43. K. Matoy, T. Detzel, M. Müller, C. Motz, G. Dehm, Interface fracture properties of thin films studied by using the micro-cantilever deflection technique. Surf. Coat. Technol. **204**, 878–881 (2009)

44. J.S.-K.L. Gibson, S. Rezaei, H. Rueß, M. Hans, D. Music, S. Wulfinghof, J.M. Schneider, S. Reese, S. Korte-Kerzel, From quantum to continuum mechanics: studying the fracture toughness of transition metal nitrides and oxynitrides. Mater. Res. Lett. **6**(2), 142–151 (2018)

45. B. Völker, C. Du, H. Fager, H. Rueß, R. Soler, C. Kirchlechner, G. Dehm, J.M. Schneider, How tensile tests allow a screening of the fracture toughness of hard coatings. Surf. Coat. Technol. **390**, 125645 (2020)

46. R. Daniel, M. Meindlhumer, W. Baumegger, J. Zalesak, B. Sartory, M. Burghammer, C. Mitterer, J. Keckes, Grain boundary design of thin films: using tilted brittle interfaces for multiple crack deflection toughening. Acta Mater. **122**, 130–137 (2017)

47. M. Bartosik, C. Rumeau, R. Hahn, Z.L. Zhang, P.H. Mayrhofer, Fracture toughness and structural evolution in the TiAlN system upon annealing. Sci. Rep. (2017). https://doi.org/10.1038/s41598-017-16751-1

48. K. Bobzin, T. Brögelmann, R.H. Brugnara, M. Arghavani, T.-S. Yang, Y.-Y. Chang, S.-Y. Chang, Investigation on plastic behavior of HPPMS CrN, AlN and CrN/AlN-multilayer coatings using finite element simulation and nanoindentation. Surf. Coat. Technol. **284**, 310–317 (2015)

49. N. Bagcivan, K. Bobzin, R.H. Brugnara, Investigation of the properties of low temperature $(Cr_{1-x}Al_x)N$ coatings deposited via hybrid PVD DC-MSIP/HPPMS. Materialwissenschaften und Werkstofftechnik **44**(8), 667–672 (2013)

50. T. Brögelmann, K. Bobzin, N.C. Kruppe, M. Arghavani, Investigation on the influence of oxygen on the deformation and cracking behavior of (Cr,Al)ON hard coatings using combinatorial static and dynamic loadings. J. Vac. Sci. Technol. A **A37**, 061509 (2019)

51. Q. Wang, F. Zhou, J. Yana, Evaluating mechanical properties and crack resistance of CrN, CrTiN, CrAlN and CrTiAlN coatings by nanoindentation and scratch tests. Surf. Coat. Technol. **285**, 203–213 (2016)

52. K. Bobzin, T. Brögelmann, N.C. Kruppe, M. Arghavani, Investigations on mechanical and tribological behavior of dcMS/HPPMS CrN and (Cr, Al)N hard coatings using nanoscratch technique. Adv. Eng. Mater. **19**(6), 1600632 (2017)

53. S. Korte-Kerzel, Microcompression of brittle and anisotropic crystals: recent advances and current challenges in studying plasticity in hard materials. MRS Commun. **7**, 109–120 (2017)

54. J.J. Guo, K. Madhav Reddy, A. Hirata, T. Fujita, G.A. Gazonas, J.W. McCauleyb, M.W. Chena, Sample size induced brittle-to-ductile transition of single-crystal aluminum nitride. Acta Mater. **88**, 252–259 (2015)

55. P.R. Howie, S. Korte, W.J. Clegg, Fracture modes in micropillar compression of brittle crystals. J. Mater. Res. **27**(1), 141–151 (2011)

56. M.F. Ashby, C.G. Sammis, The damage mechanics of brittle solids in compression. PAGEOPH **133**(3), 489–521 (1990)

57. G. Sernicola, T. Giovannini, P. Patel, J.R. Kermode, D.S. Balint, T.B. Britton, F. Giuliani, In situ stable crack growth at the micron scale. Nat. Commun. **8**(108), 1–9 (2017)

58. T.H. Sung, J.C. Huang, J.H. Hsu, S.R. Jian, Mechanical response of GaN film and micropillar under nanoindentation and micro-compression. Appl. Phys. Lett. **97**, 171904 (2010)

59. M. Birkholz, P.F. Fewster, C. Genzel, *Thin Film Analysis by X-Ray Scattering. Front Matter* (Wiley-VCH, Weinheim, 2005)

60. H. Fei, A. Abraham, N. Chawla, H. Jiang, Evaluation of micropillar compression tests for accurate determination of elastic-plastic constitutive relations. J. Appl. Mech. **79**(6), 1011–1019 (2012)

61. J. Dolbow, M. Gosz, Effect of out-of-plane properties of a polyimide film on the stress fields in microelectronic structures. Mech. Mater. **23**(4), 311–321 (1996)

62. L. Gan, B. Ben-Nissan, A. Ben-David, Modelling and finite element analysis of ultra-microhardness indentation of thin films. Thin Solid Films **290–291**, 362–366 (1996)

63. B. Moser, K. Wasmer, L. Barbieri, J. Michler, Strength and fracture of Si micropillars: a new scanning electron microscopy-based micro-compression test. J. Mater. Res. **22**(4), 1004–1011 (2016)

64. B. Daum, G. Dehm, H. Clemens, M. Rester, F.D. Fischer, F.G. Rammerstorfer, Elastoplastic buckling as source of misinterpretation of micropillar tests. Acta Mater. **61**, 4996–5007 (2013)

65. V.L. Popov, *Kontaktmechanik und Reibung—Von der Nanotribologie bis zur Erdbebendynamik*, 3rd edn. (Springer-Vieweg, Berlin, 2015)

66. T.O. Owolabi, K.O. Akande, S.O. Olatunji, Estimation of average surface energies of transition metal nitrides using computational intelligence technique. Soft Comput. **21**, 6175–6182 (2016)

67. M. Kuna, *Numerische Beanspruchungsanalyse von Rissen*, 1st edn. (Vieweg+Teubner, Wiesbaden, 2008)

68. D. Gross, T. Seelig, *Bruchmechanik*, 6th edn. (Springer Vieweg, Berlin, 2016)

69. L.J. Vandeperre, W.J. Clegg, The correlation between hardness and yield strength of hard materials. Mater. Sci. Forum **492–493**, 555–560 (2005)

70. R. Pippan, S. Wurster, D. Kiener, Fracture mechanics of micro samples: fundamental considerations. Mater. Des. **159**, 252–267 (2018)

71. A. Navarro, E.R. de los Rios, Short and long fatigue crack growth: a unified model. Philos. Mag. A **57**(1), 15–36 (2006)

72. U. Krupp, Mikrostrukturelle Aspekte der Rissinitiierung und -ausbreitung in metallischen Werkstoffen, Fachbereich Maschinentechnik der Universität Siegen, Editor. Siegen, Germany (2004)

73. S. Veprek, A.S. Argon, Towards the understanding of mechanical properties of super- and ultrahard nanocomposites. J. Vac. Sci. Technol. B **20**(2), 650–664 (2002)

74. I.A. Ovid'ko, A.G. Sheinerman, Triple junction nanocracks in deformed nanocrystalline materials. Acta Mater. **52**, 1201–1209 (2004)

75. I.A. Ovid'ko, Review on the fracture processes in nanocrystalline materials. J. Mater. Sci. **42**, 1694–1708 (2007)